Available online at www.sciencedirect.com

ScienceDirect

Progress in Natural Science: Materials International 24 (2014) 291–294

Progress in Natural Science Materials International

www.elsevier.com/locate/pnsmi
www.sciencedirect.com

Letter

Phase-field simulation of dendrite growth in the presence of lateral constraints

Lifei Du[a,b,*], Rong Zhang[a,b]

[a]Department of Applied Physics, Northwestern Polytechnical University, Xi'an 710029, China
[b]Key Laboratory of Space Applied Physics and Chemistry, Ministry of Education, Xi'an 710072, China

Received 14 November 2013; accepted 4 April 2014
Available online 2 June 2014

Abstract

The effect of a sudden change in the crossing section on the microstructural evolution as well as solute and heat diffusions during solidification of the Ni-40.8% Cu alloy was investigated by implementing a non-isothermal phase-field model. Simulations with lateral constraints of different sizes were carried out to study the changes of the dendritic growth manner. Significant changes in microstructures had been observed as the interface encountered a sharply reduced crossing section; a cellular–dendrite transition could be achieved with lateral constraints, and the tip velocity significantly changed during the development of dendrite microstructures, and also, lateral constraints of different sizes had different effects on changes of the tip positions as well as tip velocities during the dendritic growing through constraints, which agreed well with experimental results.

Keywords: Simulation and modeling; Microstructure; Solidification

1. Introduction

The properties of almost any material are mainly determined by its structure, and especially by its microstructure, which are essentially governed by phase transitions with various manufacturing processes [1–3]. In industry, many engineering components do not have a uniform cross section, and these sudden changes in crossing sections will strongly influence the heat flow in a complex geometry and the solute diffusion ahead of the interface, leading to the changes of the microstructure evolution of the solidified alloy. Therefore it is significant to elucidate the effect of discontinuities in the crossing section on the morphology evolution of the interface as well as the solute and heat diffusions. Fabietti et al. [4] investigated the effect of a sudden change in cross sections on the microstructural development by the directional solidification technique, and found that lateral constraints could significantly change the microstructure evolution as well as the solute diffusion. Wang et al. [5] carried out an experimental study on the solidification behaviors and solute redistribution of a single-crystal Nickel-based superalloy under lateral constraints, and reported the strong influence on the solidified microstructure, the solute segregation, and the solute redistribution. Besides these experimental studies, the computing simulations and modeling methods have become efficient techniques in materials science [6–9], which can provide much more information during the microstructural evolution as well as concentration and temperature distributions during the solidifying process. Phase field method, as one of the most powerful computational techniques to study phase transitions [10–12], has been widely used in solidifications [13–18]. In this paper, phase field simulations will be carried out to investigate the microstructure evolutions with lateral constraints at the interface, and the size effect of lateral constraints will be examined and discussed.

*Corresponding author at: Department of Applied Physics, Northwestern Polytechnical University, Xi'an 710029, China. Tel./fax: +86 29 88431650.
E-mail address: dulifei@mail.nwpu.edu.cn (L. Du).
Peer review under responsibility of Chinese Materials Research Society.

Production and hosting by Elsevier

http://dx.doi.org/10.1016/j.pnsc.2014.05.008
1002-0071/

2. Phase-field model and simulation method

The non-isothermal phase-field model for solidification of binary systems is implemented to simulate the microstructure evolution as well as the concentration and temperature distributions [19,20]. The main governing equations are listed below.

The phase field equation is

$$\frac{\partial\phi}{\partial t}=M_\phi\bar{\varepsilon}^2\left[\nabla(\eta^2\nabla\phi)-\frac{\partial}{\partial x}\left(\eta\eta_\beta'\frac{\partial\phi}{\partial y}\right)+\frac{\partial}{\partial y}\left(\eta\eta_\beta'\frac{\partial\phi}{\partial x}\right)\right]-M_\phi((1-x_B)H_A+x_BH_B) \tag{1}$$

The diffusion equation is

$$\frac{\partial x_B}{\partial t}=\nabla D\left[\nabla x_B+\frac{V_m}{R}x_B(1-x_B)(H_B(\phi,T)-H_A(\phi,T))\nabla\phi\right] \tag{2}$$

The temperature equation is

$$\check{c}\frac{\partial T}{\partial t}+30g(\phi)\Delta\tilde{H}\frac{\partial\phi}{\partial t}=\nabla K\nabla T \tag{3}$$

In this model, the phase-field variable ϕ varies smoothly between 0 in the solid and 1 in the liquid as assumed, x_B is the mole fraction of solute B in solvent A, T is the temperature and ε is the coefficient of gradient energy. The anisotropy of the interface energy is included by expanding $\varepsilon=\bar{\varepsilon}\eta=\bar{\varepsilon}(1+\gamma\cos\kappa\beta)$, where $\bar{\varepsilon}$ is related to the surface energy σ and interface thickness λ, γ is the magnitude of anisotropy in the surface energy, κ specifies the mode number, and the expression $\beta=\arctan((\partial\phi/\partial y)/(\partial\phi/\partial x))$ gives an approximation of the angle between the interface normal and the orientation of the crystal lattice.

The formulations included in these governing equations are as follows:

$$H_A(\phi,T)=W_Ag'(\phi)+30g(\phi)\Delta H_A\left(\frac{1}{T}-\frac{1}{T_m^A}\right) \tag{4}$$

$$H_B(\phi,T)=W_Bg'(\phi)+30g(\phi)\Delta H_B\left(\frac{1}{T}-\frac{1}{T_m^B}\right) \tag{5}$$

$$\check{c}=(1-x_B)c_A+x_Bc_B \tag{6}$$

$$\Delta\tilde{H}=(1-x_B)\Delta H_A+x_B\Delta H_B \tag{7}$$

$$K=(1-x_B)K_A+x_BK_B \tag{8}$$

where $g(\phi)=\phi^2(1-\phi)^2$, W_A and W_B are constants, T_m^A and T_m^B are the melting points of pure A and pure B, respectively. ΔH_A and ΔH_B are the heats of fusion per volume, c_A and c_B are the heat capacities, and R is the gas constant. The diffusion coefficient is postulated as a function of phase-field variables, $D=D_S+p(\phi)(D_L-D_S)$ where D_S and D_L are the classical diffusion coefficients in the solid and liquid, respectively, and $p(\phi)=\phi^3(10-15\phi+\phi^2)$ is a smoothing function with $p'(\phi)=30g(\phi)$.

The governing equations are solved using the standard finite difference method with the Tri-diagonal matrix algorithm (TDMA), and time stepping is by explicit Euler scheme. All simulations are carried out in a $1200\Delta x\times1200\Delta y$ simulation box with $\Delta x=\Delta y=0.96\lambda=4.6\times10^{-8}$ m, and the time step is $\Delta t=2.0\times10^{-8}$ s. The lateral constraint is set in the middle of the simulation zone with a height of h, an initial undercooling of ΔT, and a distance of d_1 between two constraints. All simulations are carried out for Ni–Cu binary alloy and the physical parameters are listed in Table 1. The initial concentration of the melt x_0 equals to 0.4083, and the initial temperature T_0 equals to 1574 K. The zero-Neumann boundary condition for ϕ and x_B is imposed.

Table 1
Physical parameters used in the simulations.

Parameters	Values
T_m^A – melt temperature of Ni (K)	1728.0
T_m^B – melt temperature of Cu (K)	1358.0
ΔH_A – latent heat of Ni (J/m^3)	2.35×10^9
ΔH_B – latent heat of Cu (J/m^3)	1.728×10^9
K_A – heat conductivity of Ni (W/m K)	84.0
K_B – heat conductivity of Cu (W/m K)	200.0
c_A – specific heat of Ni (J/m^3 K)	5.42×10^6
c_B – specific heat of Cu (J/m^3 K)	3.96×10^6
D_L – diffusion coefficient of the liquid phase (m^2/s)	1.0×10^{-9}
D_S – diffusion coefficient of the solid phase (m^2/s)	1.0×10^{-13}
V_m – mole volume of alloy (m^3/mol)	7.42×10^{-6}
σ_A – surface energy of Ni (J/m^2)	0.37
σ_B – surface energy of Cu (J/m^2)	0.29
β_A – interface kinetic coefficient of Ni (m/s K)	3.3×10^{-3}
β_B – interface kinetic coefficient of Cu (m/s K)	3.9×10^{-3}
λ – interface thickness (m)	4.9×10^{-8}
γ – magnitude of anisotropy	0.04

3. Results and discussions

3.1. Dendrite growth during solidification with lateral constraints

Fig. 1 shows the concentration distribution maps at the different solidifying time. Under this condition, the distance of initial cellular dendrites is $d_0=200\Delta x$ with the height of constraints $h=200\Delta x$, and the distance between lateral constraints $d_1=400\Delta x$, and the temperature of constraints is set to be 1574 K throughout the simulation. Before encountering constraints, primary cellular dendrites directly grow into the undercooled liquid melt with a steady velocity. As soon as these cellular arms contact the constraints, a part of them is completely blocked and the other part continues to grow through the distance between constraints as shown in Fig. 1(b). It is seen from Fig. 1(c) that the solid flat grows fast along constraint boundaries since these constraints are set at a fixed temperature. The new dendritic arms start to produce; hence the competitive growth between dendrites comes up to form the newly developed dendritic microstructures, as shown in Fig. 1(d), forming the mix-structure of cellular and dendrites, which is a consistent result achieved from the experiment [5]. It is intriguing that the newly formed microstructure changes from a cellular to a typical dendrite. The same phenomenon

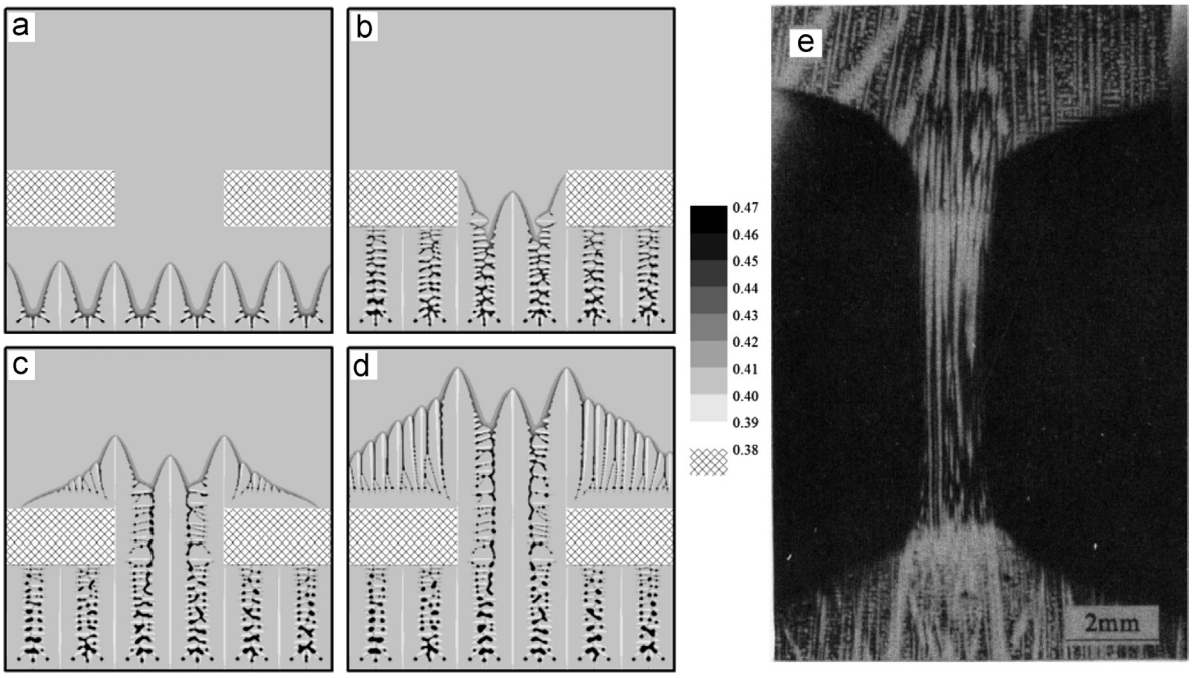

Fig. 1. Evolutions of concentration distribution during the solidification with lateral constraints. (a) 1×10^{-3} s; (b) 2×10^{-3} s; (c) 3×10^{-3} s; (d) 4×10^{-3} s; (e) experiment result [5].

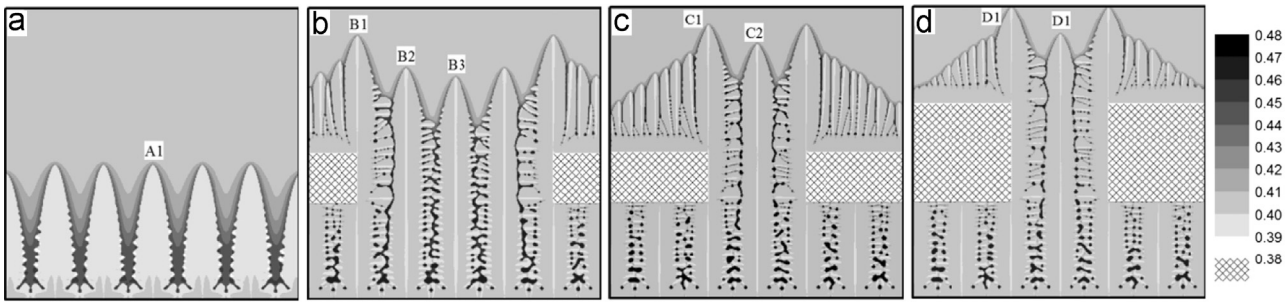

Fig. 2. Dendrite growth in the present of lateral constraints of different sizes. (a) Without constraints; (b) $d_1=200\Delta x$, $h=200\Delta x$; (c) $d_1=400\Delta x$, $h=200\Delta x$; (d) $d_1=400\Delta x$, $h=400\Delta x$.

has also been reported from experiments [4]. Finally, it is shown in Fig. 1 that the solute-trapping is restrained in the newly developed dendritic microstructure.

3.2. Size effect of lateral constraints on dendrite growth

Fig. 2 shows the concentration distribution maps at $t=4.0\times10^{-3}$ s with lateral constraints of different sizes. The change in microstructures strongly depends on the relative change in cross sections. Without lateral constraints, cellular dendrites directly grow into the undercooled melt with weak side-branching and appear strongly solute segregated. The cellular–dendrite transition can only be observed in the presence of near lateral constraints. The decreasing size of lateral constraints can constrain this transition. The increasing the size of lateral constraints can enhance the dendrite growth near these lateral constraints. The different changes in the tip growth are found with lateral constraints of different sizes. In Fig. 3, the tip positions and velocities versus time in different conditions as shown in Fig. 2 are plotted. It indicates that constraints of large height can lead to large tip velocity near constraints. Also, the tip velocity can be enhanced during the dendrites tip growing through constraints comparing with dendrite growth without lateral constraints. These results agree with experimental results [5].

4. Conclusions

A phase-field study is carried out to investigate the microstructural evolution during the solidification with lateral constraints, and the size effect of lateral constraints on the dendrite growth is studied and discussed. The main results indicate that:

(1) Lateral constraints have a significant effect on the microstructure formation during solidification. A cellular–dendrite transition can be achieved with lateral constraints,

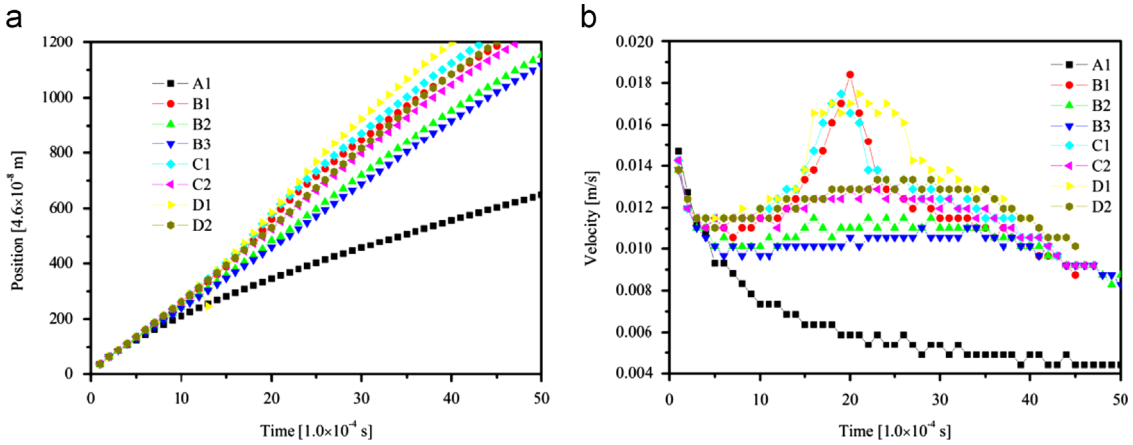

Fig. 3. Changes in (a) the positions and (b) the velocities of the dendrite tips labeled in Fig. 2.

and the solute segregation is also influenced due to the confinement effect of lateral constraints.

(2) The tip velocity of the primary dendrite arms can be enlarged during the growth of dendrite growing through lateral constraints, and the different sizes of lateral constraints have a different effect on the changes of the tip positions and velocities.

Acknowledgment

The authors gratefully acknowledge the financial support from the NPU Foundation for Fundamental Research, China [JC201272].

References

[1] M. Asta, C. Beckermann, A. Karma, W. Kurz, R. Napolitano, M. Plapp, G. Purdy, M. Rappaz, R. Trivedi, Acta Mater. 57 (2009) 941–971.
[2] H. Yasuda, T. Toh, K. Iwai, K. Morita, Isij Int. 47 (2007) 619–626.
[3] Z.M. Yan, X.T. Li, Z.Q. Cao, X.A. Zhang, T.J. Li, Mater. Lett. 62 (2008) 4389–4392.
[4] L.M. Fabietti, V. Seetharaman, R. Trivedi, Metall. Trans. A 21 (1990) 1299–1310.
[5] H.M. Wang, Y.J. Tang, J.H. Zhang, Y.A. Li, Z.Y. Zhang, Y. Yu, Z.Q. Hu, Mater. Sci. Prog. 7 (1993) 99–104.
[6] K.M. Rabe, Annu. Rev. Condens. Matter Phys. 1 (2010) 211–235.
[7] H.B. Dong, P.D. Lee, Acta Mater. 53 (2005) 659–668.
[8] E. Flenner, B. Barz, A. Neagu, G. Forgacs, I. Kosztin, Phys. Rev. E 85 (2012) 031907.
[9] G. Duggan, W.U. Mirihanage, M. Tong, D.J. Browne, IOP Conf. Ser. Mater. Sci. Eng. 33 (2012) 012026.
[10] L.Q. Chen, Annu. Rev. Mater. Res. 32 (2002) 113–140.
[11] I. Singer-Loginova, H.M. Singer, Rep. Prog. Phys. 71 (2008) 106501.
[12] I. Steinbach, Model. Simul. Mater. Sci. 17 (2009) 073001.
[13] W.J. Boettinger, J.A. Warren, C. Beckermann, A. Karma, Annu. Rev. Mater. Res. 32 (2002) 163–194.
[14] A. Karma, Phys. Rev. Lett. 87 (2001) 045501.
[15] Y.L. Tsai, C.C. Chen, C.W. Lan, Int. J. Heat Mass. Tranf. 53 (2010) 2272–2283.
[16] Z.J. Wang, J.J. Li, J.C. Wang, Y.H. Zhou, Acta Mater. 60 (2012) 1957–1964.
[17] L.F. Du, R. Zhang, H. Xing, L.M. Zhang, Y. Zhang, L. Liu, Acta Phys. Sin. 62 (2013) 106401.
[18] L.F. Du, R. Zhang, L.M. Zhang, Sci. China Technol. Sci. 56 (2013) 2586–2593.
[19] J.A. Warren, W.J. Boettinger, Acta Metall. Mater. 43 (1995) 689–703.
[20] I. Loginova, G. Amberg, J. Agren, Acta Mater. 49 (2001) 573–581.